Untangling the contributions of image charge and laser profile for optimal photoemission of high-brightness electron beams

J. Portman, H. Zhang, K. Makino, C. Y. Ruan, M. Berz, and P. M. Duxbury
Physics and Astronomy Department, Michigan State University, East Lansing, Michigan 48824, USA

(Received 20 August 2014; accepted 16 October 2014; published online 3 November 2014)

Using our model for the simulation of photoemission of high brightness electron beams, we investigate the virtual cathode physics and the limits to spatio-temporal and spectroscopic resolution originating from the image charge on the surface and from the profile of the exciting laser pulse. By contrasting the effect of varying surface properties (leading to expanding or pinned image charge), laser profiles (Gaussian, uniform, and elliptical), and aspect ratios (pancake- and cigar-like) under different extraction field strengths and numbers of generated electrons, we quantify the effect of these experimental parameters on macroscopic pulse properties such as emittance, brightness (4D and 6D), coherence length, and energy spread. Based on our results, we outline optimal conditions of pulse generation for ultrafast electron microscope systems that take into account constraints on the number of generated electrons and on the required time resolution. © *2014 AIP Publishing LLC*.
[http://dx.doi.org/10.1063/1.4900582]

I. INTRODUCTION

Time resolved imaging of materials at the single-particle or domain level can open the doors to a new understanding of a variety of interesting phenomena, from pathways in biological processes[6,13,25] to untangling electron and lattice interactions in complex materials.[3,16,18,20] In recent years, progress in high-resolution transmission electron microscopy (TEM) using coherent electron beams generated with field emission guns (FEGs) together with aberration correction, has made feasible the imaging of materials with atomic resolution.[10] Temporal resolution is harder to achieve but development of femtosecond (fs) photoemission systems retrofitted into diffraction and microscopy systems currently offer a promising technique.[23,24,26,28,33] The main challenge in this regard is represented by the so-called space charge effects,[9,22,27,30] which manifest themselves in two ways. First of all, the internal Coulomb fields of the electron pulse enhance momentum-space correlations (chirping) that act in lengthening the pulse.[27] This issue can be largely remediated in the next generation of ultrafast electron microscopes, incorporating RF cavities[30,32] which act as temporal lenses complementing the electromagnetic lenses used to focus the transverse pulse components. The second manifestation of space charge effects is of stochastic nature and provides fundamental limits to the achievable space, time, and spectroscopic resolutions in these Ultrafast Electron Microscopes (UEMs). This stochastic space charge effect is caused by an irreversible growth in rms beam emittance due to fluctuating components of the nonlinear electron dynamics, an issue also present in TEM systems at strong beam crossovers.[5] In the UEMs, it is correlated with virtual cathode (VC) formation during the electron pulse generation, due to the negative charge of the electrons emitted during the early stages of the photoemission process and the attractive image charge field on the photocathode surface. This results in an increased fraction of recombined electrons and in a degradation of pulse properties once the critical current corresponding to the VC limit has been reached.[31] This value is a function of the extraction field and of the properties of the photoemitting laser and surface.

The goal of this paper is to untangle the contributions originating from the image charge on the surface and from the spatio-temporal profile of the laser pulse and to give guidelines for optimal pulse generation that would reduce the stochastic space charge effect and be tailored to different experimental realizations. We extend our previous work[19] on the state-of-the-art multiple level fast multipole method (MLFMM) simulation technique used to describe photoemission with a Gaussian laser pulse, to include varying laser pulse shapes (uniform and elliptical), with the corresponding image charge fields generated on the surface. In addition to considering the effect that shaping the laser pulse has on the onset of the virtual cathode, we include effects due to the pinning of the image charge onto a confined area on the surface as a simplified model for a patterned photocathode. We also vary the aspect ratio of the photoemitting laser pulse from a pancake to a cigar shape and discuss the pulse properties associated with each. We conclude with a discussion of the limits of the temporal and spatial resolutions in the different configurations analyzed in the presence of image charge and define optimal conditions of pulse generation that take into account the number of electrons and the requirements on the spatial and temporal resolutions. We note here that traditionally in the field,[14] the normalized root-mean-square (rms) emittance projected onto the longitudinal or transverse directions (Eq. (6)) is used as a figure of merit to compare different schemes of pulse generation. However, according to Liouville's theorem, only the true 6D emittance is conserved, but this quantity is prohibitive to compute in a simulation and not accessible experimentally. Therefore, while we include the emittance data in our discussion to allow comparison with previous literature, we suggest that other quantities such as the temporal and spatial resolutions at the sample, offer a more robust figure of merit and should be used when evaluating source performance.

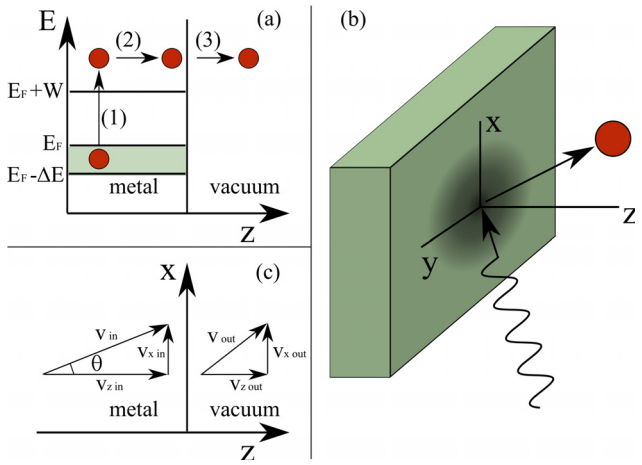

FIG. 1. (a) Schematic of the three-step photoemission model: (1) the electron absorbs a photon of energy $\hbar\omega$, (2) migrates to the surface, and (3) escapes to the vacuum. (b) Definition of the coordinate system used in the simulation. Also shown is the Gaussian profile of the laser pulse on the photocathode surface. (c) Diagram showing the velocity of the electron inside the metal and in vacuum. Notice the conservation of transverse velocity across the interface and the decrease of the velocity in the perpendicular direction, v_z due to the potential barrier at the surface.

II. METHODS

We wish to briefly review the simulation method used in the present work. In the UEM system, the electron bunch is generated through photoemission from a gold photocathode irradiated with a fs laser pulse. This process can be described using the so-called three-step photoemission model[4,7] in which each electron is emitted independently as a result of absorbing a photon of energy $\hbar\omega$, diffusing to the surface and escaping to the vacuum [Fig. 1(a)]. If the photon energy is higher than the gold work function, $W = 4.0 - 4.6\,\text{eV}$,[1,12,21,29] a fraction of the electrons inside the metal can absorb enough energy to overcome the potential barrier and escape to the vacuum. The energy difference, $\Delta E = \hbar\omega - W$, allows only electrons with energies in the range $[E_F - \Delta E, E_F]$ to be emitted, and since typically ΔE is small compared to the Fermi energy E_F, the generated bunch has a narrow energy spread. We assume a uniform distribution of states within this energy band. The physical parameters used to describe the system in the simulations are summarized in Table I.

The initial velocities of the electrons are calculated taking into account that in order to escape the photocathode the electrons need to have enough energy to overcome the work function of the material. Taking z as the direction perpendicular to the photocathode surface [Fig. 1(b)], this results in the following equations for the initial velocities:[7]

TABLE I. Physical parameters used in the simulation.

Fermi energy, E_F	5 eV
Work function, W	4.45 eV
Photon energy, $\hbar\omega$	4.66 eV
Laser pulse duration, Δt	50 fs (pancake)
	10 ps (cigar)
Laser pulse width, σ_r	91 μm (pancake)
	9.1 μm (cigar)

$$v_{x;out} = v \sin\theta \cos\phi, \tag{1}$$

$$v_{y;out} = v \sin\theta \sin\phi, \tag{2}$$

$$v_{z;out} = \sqrt{(v\cos\theta)^2 - 2(E_F + W)/m_0}, \tag{3}$$

where $v = \sqrt{\frac{2(E_i+\hbar\omega)}{m_0}}$, m_0 is the rest mass of the electron, the initial energy $E_i \in [\text{EF} - \Delta\text{E}, \text{EF}]$, $\theta \in [0, \theta_{\max}]$ and $\phi \in [0, 2\,\pi]$. $\theta_{\max}$, similar to the angle of total internal reflection in classical optics, quantifies the maximum angle for which the electron can escape with sufficient velocity in the z direction and is given by

$$\cos\theta_{max} = \frac{v_{z\,min}}{v} = \sqrt{\frac{E_F + W}{E_i + \hbar\omega}}. \tag{4}$$

The initial coordinates in directions parallel to the surface (x, y in our notation) are randomly generated given the spatial profile of the laser pulse and the initial z coordinate is set equal to zero.

To treat the time evolution of the emitted electrons, their relativistic equations of motion are solved at each time step using a fourth order Runge-Kutta algorithm. The particles that fall back on the surface ($z < 0$) are removed from the simulation and collisions between electrons are avoided by imposing a maximum force cutoff. To calculate the Coulomb forces felt by the electrons, we have used COSY INFINITY,[15] which treats the space charge effects with a MLFMM.[34] This approach gives an algorithm that scales almost linearly with the number of particles with a prefactor that depends on the multipole order used. To further reduce the computational time and allow simulations with higher numbers of electrons, we use macroparticles so that typically one simulated particle corresponds to 100 electrons.

Each emitted electron contributes to the formation of an image charge on the surface of the photocathode, which has to be included in the simulation due to its strength F_s being of the same order of magnitude of the extraction field F_a, with $F_s = N_e^{emit}/[\pi 2\ln(2)\sigma_r^2] \simeq 10\text{MV/m}$, where σ_r denotes the laser pulse width. To do so, we approximate the field on the surface with a continuous distribution and calculate its strength by dividing the surface into N_r rings with charge

$$Q_i = Q \int_0^{2\pi} d\theta \int_{r_{i,int}}^{r_{i,ext}} dr\, r \cdot f(r), \tag{5}$$

where $i = 1,\ldots, N_r$, Q is the total charge in the pulse, $f(r)$ is the normalized charge distribution on the surface, proportional to the laser intensity and the system has been assumed radially symmetric. $r_{i,ext}$ and $r_{i,int}$ indicate, respectively, the outer and inner radius of the ith ring and since the width of each ring $\Delta r = r_{i,ext} - r_{i,int} \ll \sigma_r$, we can approximate each one with an infinitesimally thin ring of charge located at $r_{i,0} = (r_{i,int} + r_{i,ext})/2$ with charge Q_i. The total electric field due to this image charge is then calculated as a sum of the field generated by each ring i using the well known equation for a uniformly charged ring.[11] Details on the spatial laser pulse shape enter in the calculation through the function $f(r)$ that specifies the charge distribution on the surface and

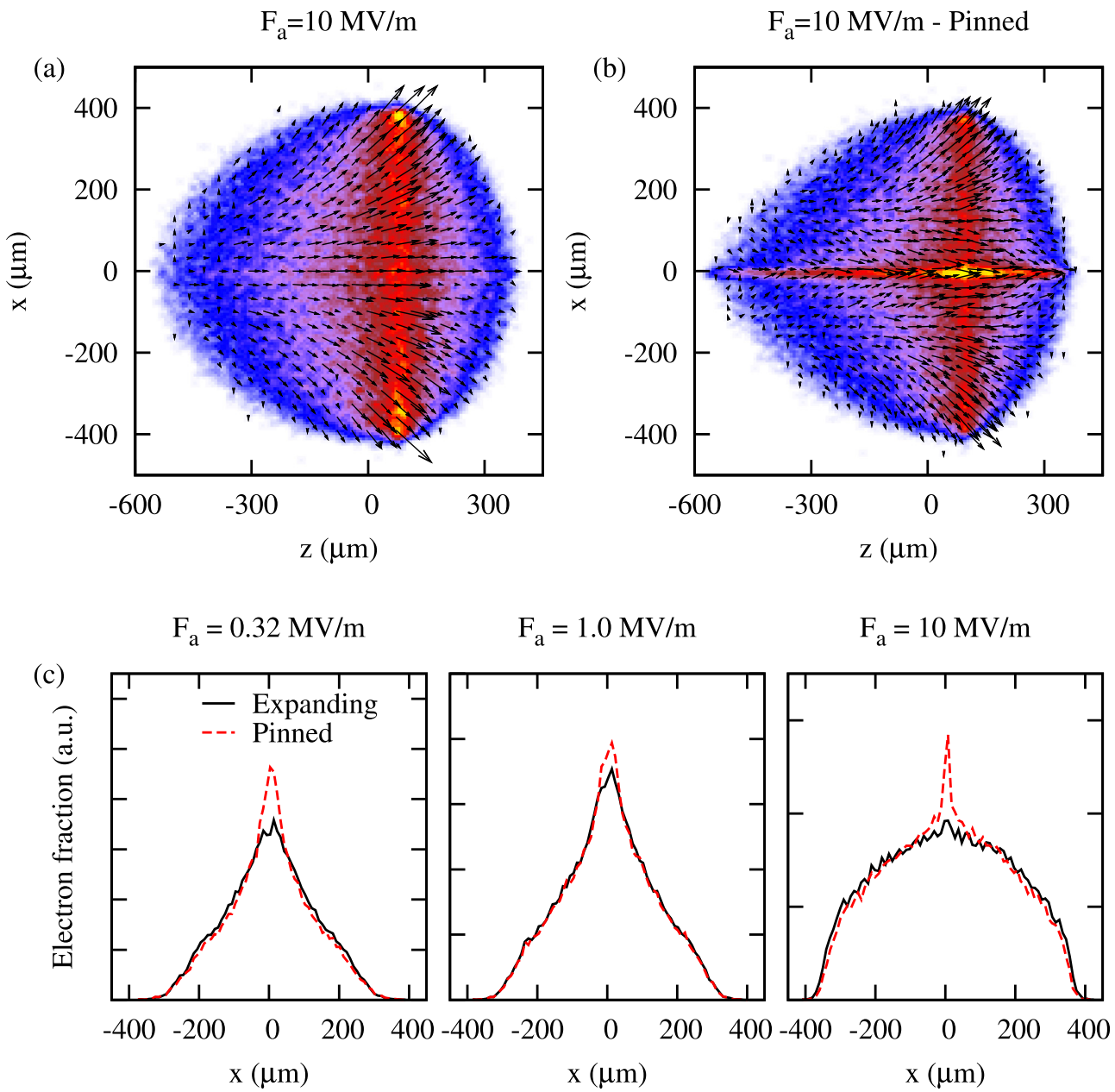

FIG. 2. (a) and (b) Color map of the charge distribution in the rest frame of the bunch projected onto the x-z plane, overlaid with arrows representing the average electron velocity. Panel (a) shows the distribution at $t = 120$ ps for extraction field $F_a = 10$ MV/m and number of emitted electrons $N_e^0 = 7 \times 10^6$. Panel (b) shows the charge distribution under the same conditions with the image charge pinned to a small area on the photocathode surface. (c) Transverse charge density profiles under different extraction fields ($F_a = 0.32$, 1, and 10 MV/m) showing the central focusing peak caused by the pinned image charge.

determines the charge of each ring Q_i. Note that the magnitude of the positive charge on the surface depends on the number of electrons in the pulse and is therefore reduced by electron recombination.

In our code, the electric field due to the image charge is calculated on a mesh with linear interpolation of the field between the mesh points. To allow electron extraction and keep the longitudinal component of field on the surface [$E_z(z = 0)$] finite, we set it equal to zero. The accuracy of this approach was confirmed by both changing the mesh size and by placing the positive field behind the surface at a distance $z = -z_{CM}$, where z_{CM} is the distance of the center of mass of the electron pulse from the surface (see Fig. 7 and the discussion in the text).

Since in the initial stages of the photoemission process the shape of the extracted electron pulse mirrors the profile of the laser pulse, this is naturally the case also for the image charge on the surface. Given its spatial width on the surface, $R_0(t)$, we have that $R_0(t = 0) = \sigma_r$. In general $R_0(t)$ will have a complex dependence on the instantaneous shape of the emitted pulse and on the cathode properties, as both surface characteristics and material thickness play a role in determining the image charge created by the electrons. To treat this in our simulations, we consider two types of systems. If the positive charges are pinned on the surface, as would be the case, for example, in a patterned photocathode, the expansion of R_0 will be hindered or even blocked. We approximate these cases by taking $R_0(t) = R_0(t = 0)$, so that the image

charge is pinned to a small constant area on the surface corresponding to its initial value. On the other hand, if the positive charges on the surface are able to expand and mirror the dynamics of the electron pulse, such as for a flat metal surface, the charge radius $R_0(t)$ will increase as the electron pulse spreads. To first order this can be approximated by taking the standard deviation of the surface charge distribution equal to the instantaneous transverse width (standard deviation) of the electron pulse.

In addition to the Coulomb electron-electron forces and the field due to the image charge, a constant electric field is applied in the direction perpendicular to the photocathode surface. Typical values for extraction fields are between 0.1 and 1 MV/m for the thermionic gun geometry,[10] between 1 and 10 MV/m for the DC electron gun,[28] and between 10 and 100 MV/m for the RF gun.[2] To provide relevant data over the whole range, we vary the extraction field between 0.1 MV/m and 10 MV/m which corresponds to generation of electrons with energies ranging from 5×10^{-3} keV to 100 keV at t = 120 ps.

III. OPTIMIZING THE PHOTOEMISSION CONDITIONS

To elucidate the effects of the expansion of image charge and the spatial and temporal photoemission laser profiles on the stochastic emittance increase and pulse resolution, we perform N-particle simulations using the method described above to model the time evolution of the generated electron pulse. In particular, we wish to understand the optimal pulse generation conditions with a given number of electrons or, equivalently, laser fluence, and extraction field. In our previous work, we validated the simulation method by comparing with numerous experimental parameters,[19] showing that our model can accurately describe the physics of the photoemission process and provide a useful tool to guide researchers in the choice of optimal electron source parameters.

A. Effect of image charge pinning

To understand the effect of photocathode geometry, we begin our discussion by looking at the effect that pinning the image charge on the surface has on the onset of the virtual cathode (VC) limit and on the final pulse parameters. Using a Gaussian laser pulse, we simulate the time evolution of pulses both with and without charge pinning and observe that in the pinned case the field on the photocathode surface provides a focusing effect which is absent for the expanding field [Figs. 2(a) and 2(b)]. As a consequence, the fraction of electrons at the center of the pulse is increased [Fig. 2(c)] at the expense of the density of electrons in the lateral regions. In addition, the pinned field generates an attractive force that at low extraction fields prevents the pulse from fully detaching from the surface even at $t = 120$ ps.

To consider the effect that charge pinning has on the scaling of the macroscopic pulse parameters, it is useful to define two regimes of electron source operation:[31] below the so-called Virtual Cathode (VC) limit, the number of electrons emitted is linearly dependent on laser fluence, and the properties of the pulse are relatively insensitive to the details of the image charge field. Approximately the same number of electrons is emitted from the surface for both treatments of the image charge field and a small (<1%) increase in the longitudinal width is observed in the presence of pinning. The onset of the VC limit is marked by a deviation from the linear scaling between laser fluence and number of electrons emitted due to a buildup of charge that hinders further electron emission. Above the VC limit, the charge pinning scenario shows a stronger electron recombination so that the final N_e^{emit} is about 5% less than in the expanding field case. These observations are confirmed by the data relative to the 6D normalized rms pulse emittance (Fig. 3), defined as

$$\epsilon_x = \frac{1}{m_0 c}\sqrt{\langle x^2\rangle\langle p_x^2\rangle - \langle x p_x\rangle^2}, \tag{6}$$

$$\epsilon_{6D} = \epsilon_x \cdot \epsilon_y \cdot \epsilon_z. \tag{7}$$

We note that ϵ_{6D} is an approximation of the true 6D emittance neglecting correlations between the x, y, and z directions. We calculate this quantity as traditionally the emittance has been used as a key figure of merit for UEM systems, being an estimate of the phase space occupied by the pulse and therefore setting limits on the achievable resolution.[19] The results in Fig. 3 show an overall increase of the 6D emittance upon the onset of the VC regime, with the pinned charge scenario showing one order of magnitude higher values of emittance in this region, while below the VC (low N_e^{emit}) charge pinning has little to no effect.

B. Effect of transverse laser pulse shape

We now turn our attention to the effect of the laser pulse shape on the properties of the photoemitted electron pulse and start by observing the temporal evolution of an electron bunch generated from an elliptical laser pulse [Figs. 4(a) and 4(b)], with the laser intensity on the surface $I(r) \propto \sqrt{1-(r/R)^2}$, where R corresponds to the spatial width of the laser. Also shown for comparison is the time evolution of a similarly generated pulse in the absence of the

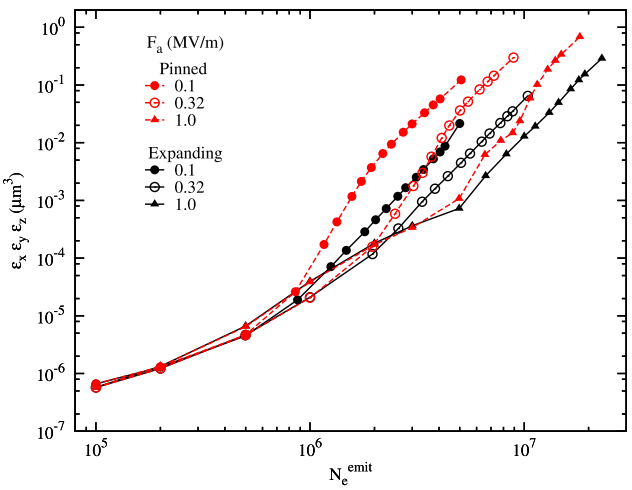

FIG. 3. 6D emittance dependence on number of emitted electrons N_e^{emit} and extraction field F_a with both pinned (red lines and symbols) and expanding surface charges (black lines and symbols).

surface image charge [Figs. 4(c) and 4(d)]. Similar to the pinned case, the positive field on the surface attracts the electrons and causes a focusing of the electron density towards the center of the pulse where the field is strongest. For the elliptical profile, we also observe a dramatic change in the overall pulse shape that is a consequence of the drastic disruption of the linear self fields otherwise present in the elliptical pulse.[14] Projecting the charge distribution onto the x-axis [Fig. 4(e)] show this effect in the formation of a pronounced central peak and a fit of the data to Gaussian and

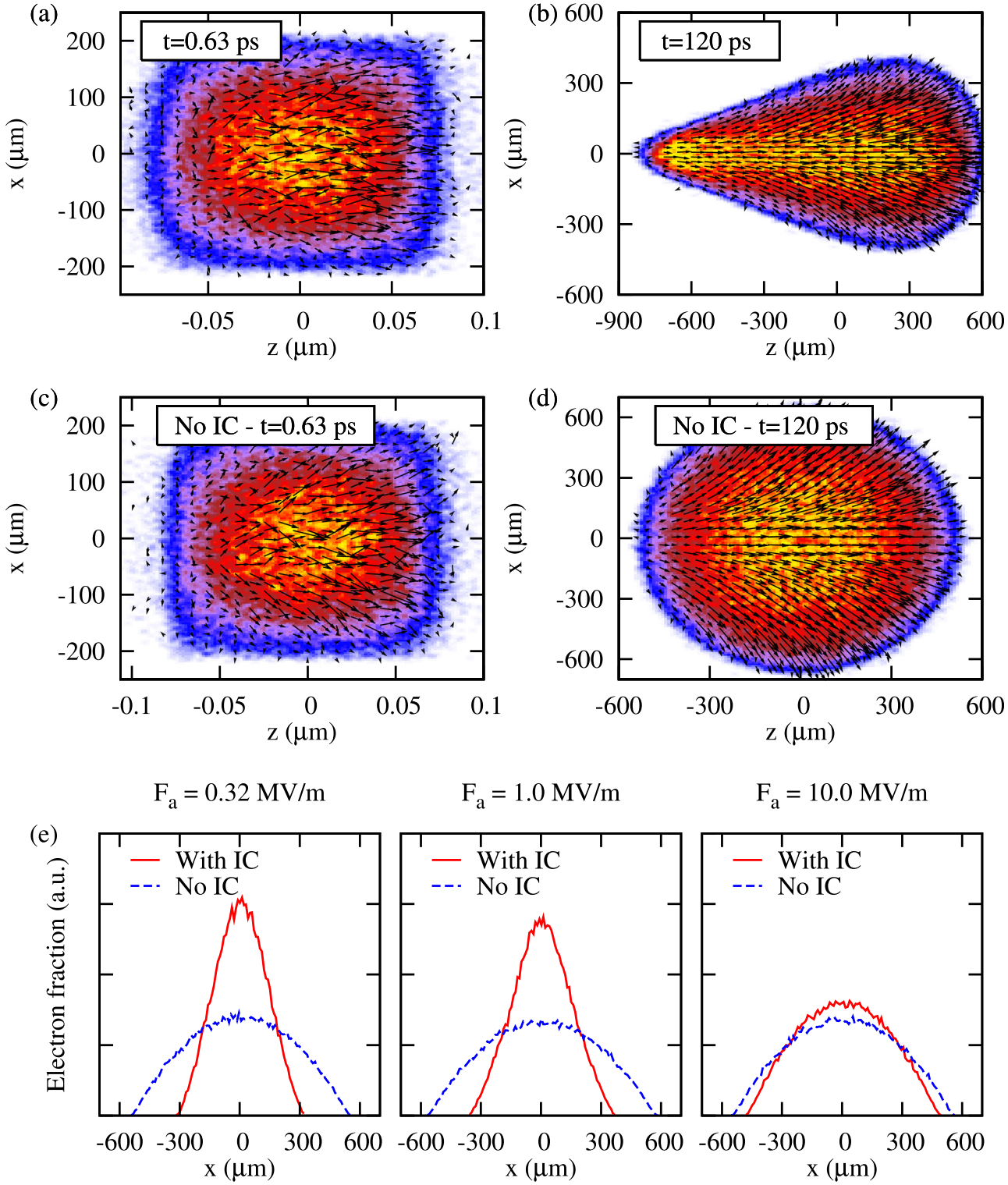

FIG. 4. (a)–(d) Color map of the charge distribution in the rest frame of the bunch projected onto the x-z plane, overlaid with arrows representing the average electron velocity for the elliptically shaped pulse. Panels (a) and (b) show the initial and final stages of photoemission in the presence of an expanding image charge on the surface. Panels (c) and (d) correspond to the case without image charge. Note that the initial number of electrons is the same in all cases, $N_e^0 = 1 \times 10^7$, with an extraction field $F_a = 1$ MV/m. (e) Transverse charge density profiles under different extraction fields ($F_a = 0.32$, 1, and 10 MV/m), with and without image charge.

elliptical distributions shows an increasing weight of the Gaussian pulse component at low extraction fields (67% at $F_a = 0.32$ MV/m and 37% at $F_a = 10$ MV/m) for which the perturbation to the pulse profile is more pronounced as the electrons remain closer to the surface throughout the simulation. Similar results (not shown) are seen using a uniform (top-hat) laser pulse [$I(r) \propto const$ for $r < R$].

Changing the shape of the laser profile used to emit the electrons also has a significant impact on the rms emittance (Fig. 5). For $F_a = 1$ MV/m (black symbols and lines), the elliptical shape (circles) is favorable below the VC limit as it has a smaller transverse emittance [panel (a)] compared to the Gaussian and uniform (top-hat) profiles. Previous literature[14,17] showed this to be the case for negligible image charge fields due to the internal linear self-forces that limit the increase of the emittance. It is non-trivial that this would still be the case even in the presence of the positive field on the surface, which disrupts the linearity of the electron-electron forces and drastically changes the resulting pulse profile (Fig. 4). The results in Fig. 5 show that once the VC limit is reached, at about $N_e^{emit} \simeq 1 \times 10^7$ for $F_a = 1$ MV/m, both the elliptical and uniform profiles present a sharp scaling with the number of electrons, while the Gaussian profile retains a more favorable scaling, with a slope for the emittance increase that is 1/3 that of the elliptical case. The origin of this can be understood by looking at the inset in Fig. 5, which presents the number of emitted electrons N_e^{emit} as a function of N_e^0, the initial number of electrons. In the elliptical and uniform case, the VC effect completely blocks the increase in N_e^{emit}, such that for $N_e^0 > 10^7$, the curves shown in the inset are flat. With a Gaussian laser profile, due to its longer tails, the emission of electrons is instead only hindered allowing an extraction of a higher number of particles under the same conditions. An increase in the extraction field F_a has the effect of shifting the onset of the VC regime to higher N_e^{emit}, thus increasing the regime before the VC is reached in which the elliptical pulse is optimal. The longitudinal emittance ϵ_z [Fig. 5(b)] scales linearly with the number of electrons for all laser profiles considered, with a weak dependence on the extraction field. The signature of the onset of the VC regime is also seen here in the sudden increase of ϵ_z by about one order of magnitude for $N_e^{emit} \simeq 1 \times 10^7$.

The influence of the image charge on the emittance can be understood by comparing the time evolution of the 6D normalized emittance ($\epsilon_x \cdot \epsilon_y \cdot \epsilon_z$) as a function of laser pulse profile and presence of image charge, shown in Fig. 6 both below and above the VC limit. Below the virtual cathode limit [Fig. 6(a)], the image charge acts as a weak perturbation on the pulse dynamics with some effect only during the initial stages ($t < 60$ ps) of pulse formation. In contrast, for extraction conditions above the virtual cathode limit [panel

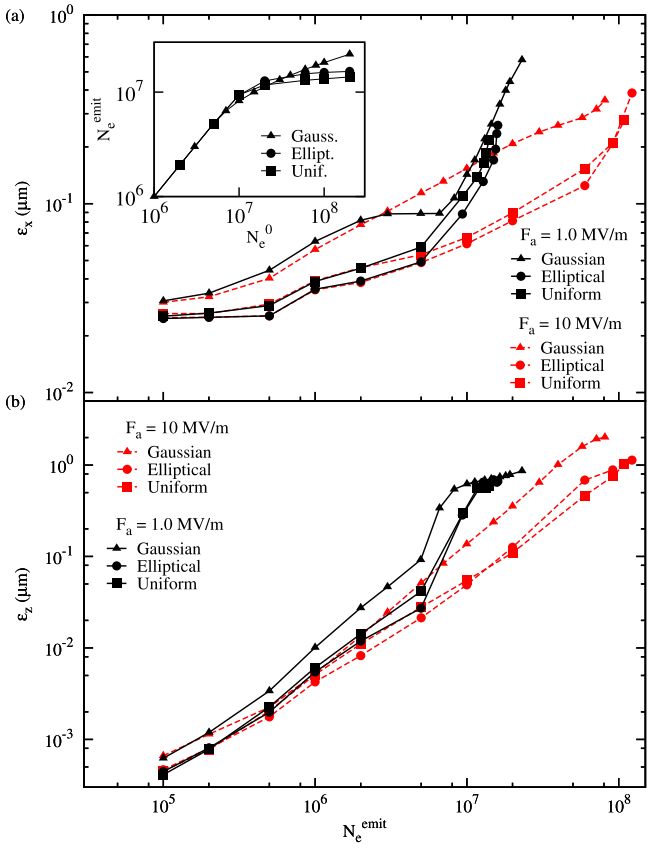

FIG. 5. (a) Transverse normalized rms emittance ϵ_x and (b) longitudinal normalized rms emittance ϵ_z dependence on number of emitted electrons N_e^{emit} and extraction field F_a for varying shapes of the exciting laser pulse at $t = 120$ ps. Inset: number of emitted electrons N_e^{emit} at $t = 120$ ps as a function of N_e^0, the initial number of electrons for $F_a = 1$ MV/m and varying laser profile.

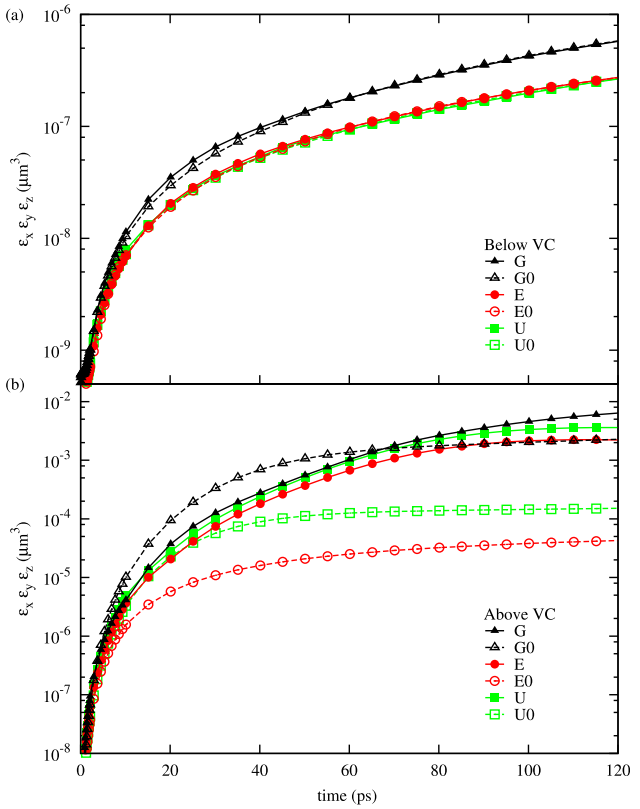

FIG. 6. Time dependence of the 6D normalized rms emittance for $F_a = 1$ MV/m both (a) below and (b) above the virtual cathode limit. The data shown corresponds to the Gaussian (G), Elliptical (E), and Uniform (U) cases, with the subscript 0 indicating the absence of the image charge (G0, E0, U0, respectively).

(b)], the strong positive field on the surface has a small effect on the emittance of the Gaussian pulse profile (black continuous and dashed lines) but is a significant perturbation in both the elliptical (red) and uniform (green) pulses.

From this, we can conclude that the optimal extraction conditions depend on a delicate balance between the image charge, which disrupts the favorable internal self-fields of both the elliptical and uniform cases, the number of electrons emitted, and the extraction field, which controls the onset of the virtual cathode limit. Below this limit, the image charge has a weak effect with the pulse properties primarily controlled by the laser parameters (laser profile and fluence), while above the VC limit the image charge strongly perturbs the expansion of the pulse with a nonuniform dependence on the pulse profile.

A further check of these considerations is shown in Fig. 7 where the 6D emittance is plotted as a function of time for the Gaussian and elliptical cases using different models for the image charge: expanding radially, pinned, and placed behind the surface at a distance $z = -z_{CM}$, where z_{CM} is the distance of the center of mass of the electron pulse. Below the virtual cathode limit, the emittance values are robust with respect to the different choices in treating the image charge. On the other hand in the nonlinear regime shown by the pulse above the VC limit, the choice of the model for the image charge can have the effect of varying

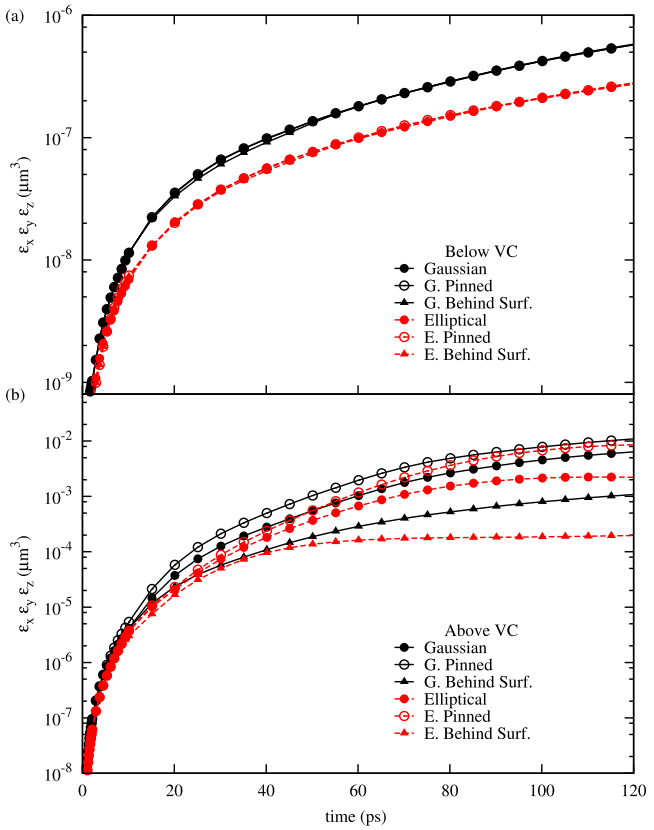

FIG. 7. Time dependence of the 6D normalized rms emittance for $F_a = 1$ MV/m both (a) below and (b) above the virtual cathode limit. The data shown correspond to the Gaussian (G) and Elliptical (E) cases, for different ways of considering the image charge field: expanding, pinned to the surface or mirroring the electron pulse distance from the surface.

the final value of emittance by about 2 orders of magnitude for the elliptical case and by about one for the Gaussian profile. Conventionally, UEM systems always operate below the VC regime where the image charge field does not have a critical effect, but this raises an important issue that needs to be addressed in pushing to higher brightness electron pulses.

C. Effect of laser pulse duration—Cigar vs Pancake

The aspect ratio of the laser pulse also has important effects on the properties of the photoemitted electron bunch in the presence of strong image charge. Our discussion so far has focused on the so-called pancake regime, characterized by a laser pulse in which the transverse width is greater than the longitudinal one, $\sigma_T \gg \sigma_z$. The cigar regime on the other hand is characterized by an elongated pulse in which $\sigma_z \gg \sigma_T$ and has been suggested[8] as a promising choice to improve the extraction efficiency by shifting the onset of the VC at the expense of the temporal resolution. In our simulations, already after 50 ps [Fig. 8(b)] the cigar shaped pulse has assumed the typical elongated aspect ratio with $\sigma_T/\sigma_z \simeq 0.13$. For comparison, the aspect ratio of a pulse in the pancake regime in our simulations under similar conditions is $\sigma_T/\sigma_z \simeq 2.5$. Due to the internal dispersive forces, the time evolution of the cigar-like pulse is characterized by an expansion both in the longitudinal and transverse directions which in our simulations leads to a constant aspect ratio [Figs. 8(c) and 8(d)].

This feature of the cigar shaped pulse leads to a lower transverse thermal emittance below the virtual cathode limit [Fig. 9(a)] with a strong dependence on N_e^{emit} and a rapid increase once the VC regime is reached. The number of electrons extracted [inset of Fig. 9(a)] increases as a function of fluence (or, equivalently N_e^0) and shows a steep increase even after the VC, so that at high N_e^0 (not shown in the figure) a higher charge is extracted than in the pancake regime, in agreement with the observations by Filippetto *et al.*[8] The drawback of this approach is due to the elongated nature of the cigar aspect ratio, causing a higher longitudinal emittance [Fig. 9(b)] and with a scaling opposite to that of the pancake regime: a weak dependence on the number of emitted electrons and a strong scaling with the extraction field.

IV. GUIDELINES FOR GENERATION OF HIGH BRIGHTNESS ELECTRON BEAMS

To conclude our discussion and extract useful guidelines for electron beam generation, we compare the brightness (Fig. 10), coherence length and energy spread (Fig. 11) for pulses generated under the different conditions described in Secs. III A–III C. In particular, we compare the Gaussian and Elliptical shapes in the pancake regime to a cigar-like pulse (see Table I). Since pinning of the image charge on the surface has a negligible effect below the VC and an unfavorable scaling after the VC, it has been omitted for clarity from the discussion that follows.

The first parameters we wish to look at are the 4D and 6D brightness defined as $B_{4D} = N_e/(\epsilon_x \cdot \epsilon_y)$ and $B_{6D} = N_e/(\epsilon_x \cdot$

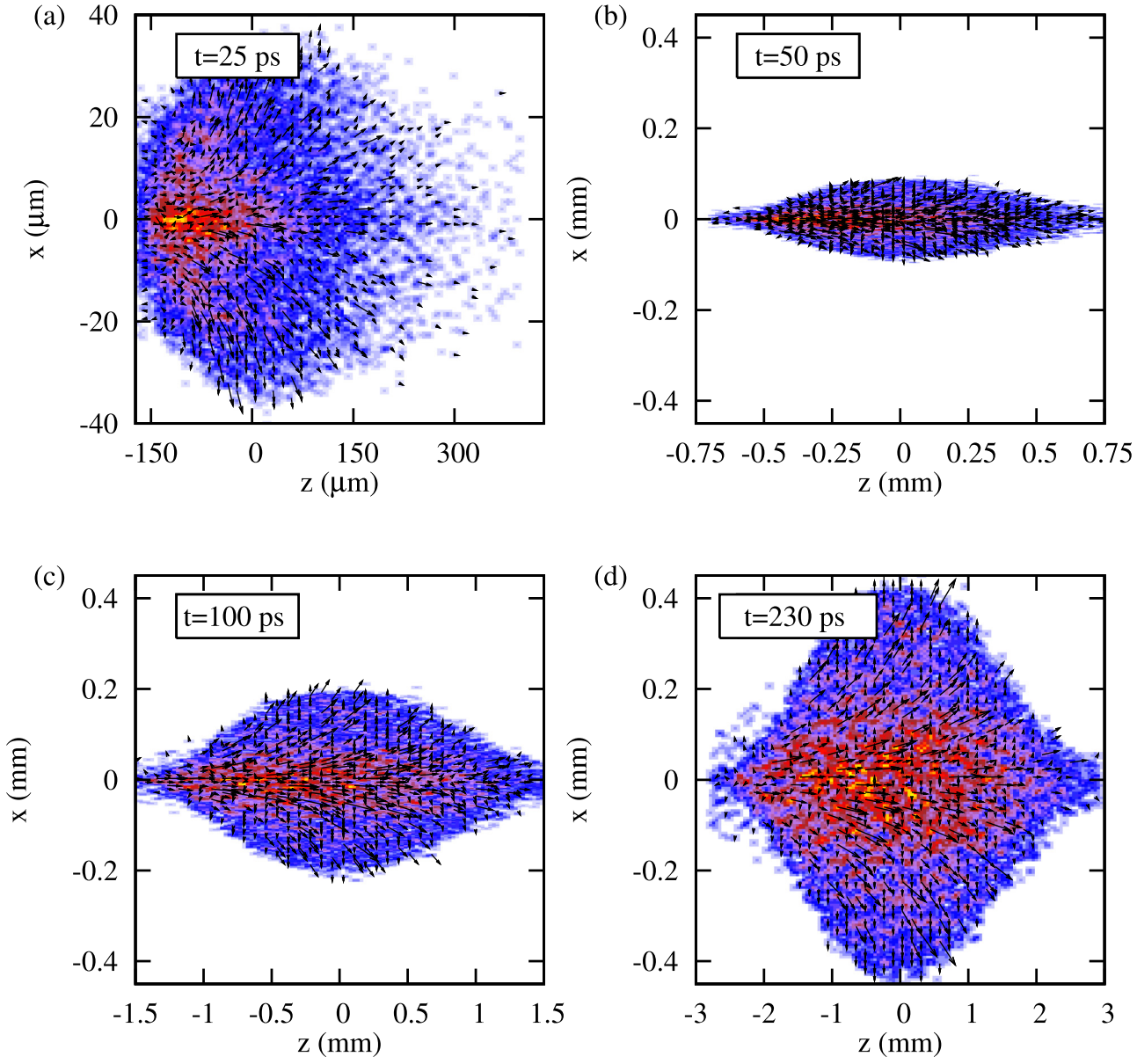

FIG. 8. (a)–(d) Color map of the charge distribution in the rest frame of the bunch projected onto the x-z plane, overlaid with arrows representing the average electron velocity for the cigar shaped pulse at different times, with $N_e^0 = 1 \times 10^6$ and extraction field $F_a = 10$ MV/m.

$\epsilon_y \cdot \epsilon_z$), reported in Fig. 10. If temporal resolution is not required, the appropriate figure of merit is the 4D brightness [panel (a)], where we observe three distinct regimes for a given extraction field F_a. At low pulse currents ($N_e < 5 \times 10^5$ for $F_a = 1$ MV/m), the cigar shape offers distinctly higher brightness than either the Gaussian or Elliptical pancake-like profiles. For intermediate values of N_e ($5 \times 10^5 < N_e < 3 \times 10^7$ for $F_a = 1$ MV/m), a pancake aspect ratio with an elliptical spatial profile seems to offer the best compromise, with a peak brightness that is lower than that achievable with the cigar-like pulse. At high numbers of electrons ($N_e > 3 \times 10^7$ for $F_a = 1$ MV/m), the Gaussian pulse offers a better scaling than the Elliptical or cigar-like pulses but is associated with a very low peak brightness. Increasing the extraction field solves this issue by shifting the boundaries between the regimes discussed to higher values of N_e. On the contrary, if temporal resolution is a concern, it is necessary to include the longitudinal pulse properties in the discussion and therefore the 6D brightness is the relevant figure. From our results in Fig. 10(b), we conclude that in this case a pancake like pulse with an elliptical transverse profile offers the optimal choice for the whole parameter range considered.

Other key quantities for electron source design are the coherence length, defined as

$$L_C = \frac{h}{2m_0 c}\frac{\sigma_x}{\epsilon_x}, \tag{8}$$

where σ_x is the transverse pulse width and h is Planck's constant, and the energy spread

$$\Delta E = \frac{\epsilon_z}{\Delta t} m_0 c, \tag{9}$$

with Δt corresponding to the temporal pulse duration. These two quantities are plotted in Fig. 11 as a function of emitted

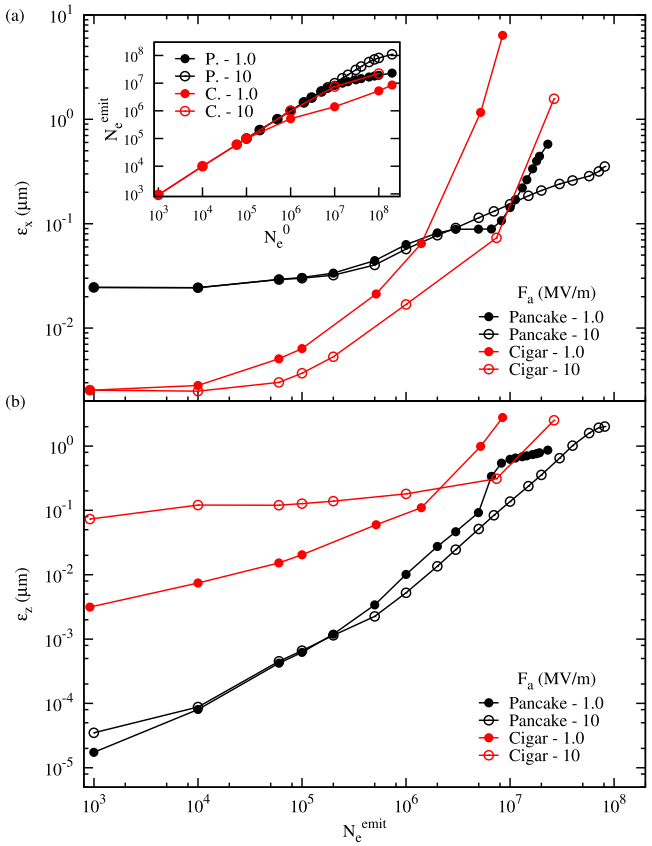

FIG. 9. (a) Transverse normalized rms emittance ϵ_x and (b) longitudinal normalized rms emittance ϵ_z dependence on number of emitted electrons N_e^{emit} and extraction field F_a for the pancake and cigar pulses. Inset: number of emitted electrons N_e^{emit} as a function of N_e^0, the initial number of electrons for $F_a = 1$, 10 MV/m and varying aspect ratio.

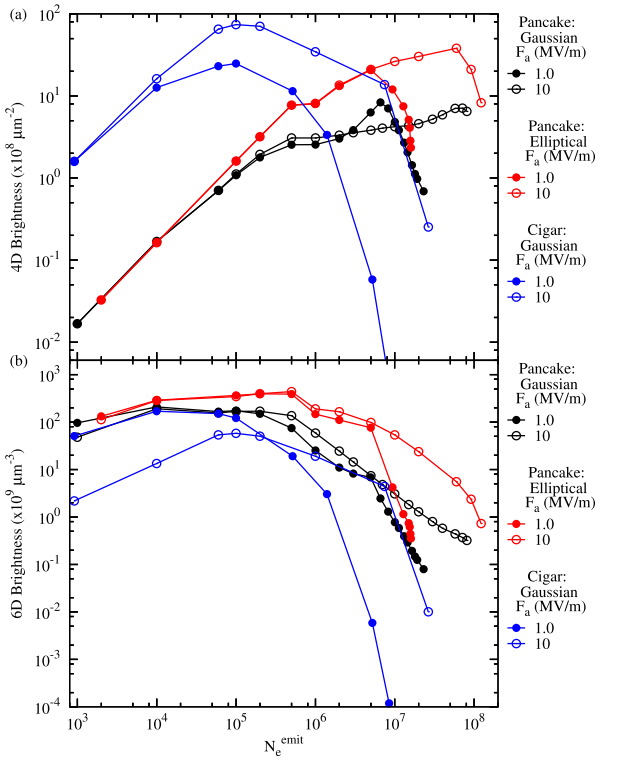

FIG. 10. (a) 4D brightness and (b) 6D brightness as a function of number of electrons emitted, N_e^{emit} for the pancake (Gaussian and Elliptical in black and red, respectively) and cigar (blue) aspect ratios. The data shown corresponds to $F_a = 1.0$ MV/m (closed circles) and $F_a = 10$ MV/m (open circles).

electron number and photoemitting laser pulse shape. The cigar-like pulse presents significantly better coherence length than the other two data sets until reaching the VC limit. Increasing the extraction field does not offer many advantages in this case since, while it pushes the onset of the VC limit to higher N_e, it also lowers the coherence length obtained. The cigar-like pulse is also favorable in terms of presenting a lower energy spread ΔE at low extraction fields (Fa = 1 MV/m but due to the linear scaling of its longitudinal emittance with the extraction field, a higher Fa leads to an increased ΔE, which can exceed the value obtained with the pancake-like Gaussian or Elliptical profiles.) but due to the linear scaling of its longitudinal emittance with the extraction field, a higher F_a leads to an increased ΔE, which can exceed the value obtained with the pancake-like Gaussian or Elliptical profiles.

V. CONCLUSIONS

Our results show that the optimal electron pulse generation regime depends on the number of electrons needed in a single pulse. By operating in the pancake regime below the VC limit, the emittance can be optimized by using an elliptical laser pulse. In this regime, the radial expansion of the image charge field has little influence on the final electron

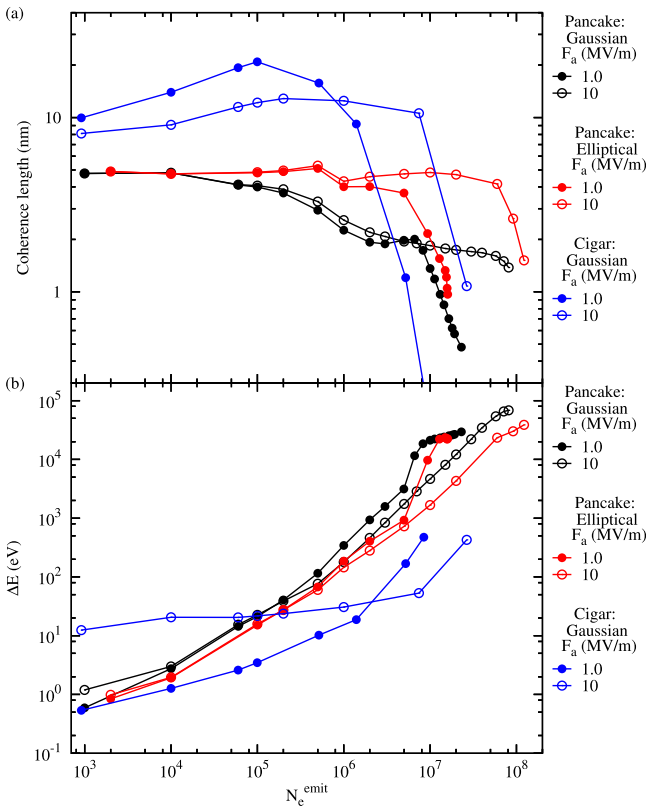

FIG. 11. Coherence length (a) and energy spread (b) as a function of number of electrons emitted, N_e^{emit} for the pancake (Gaussian and Elliptical in black and red, respectively) and cigar (blue) aspect ratios. The data shown corresponds to $F_a = 1.0$ MV/m (closed circles) and $F_a = 10$ MV/m (open circles).

bunch characteristics with the pinned and radially expanding fields showing similar pulse parameters. In the VC regime, properties of the extracted bunch strongly depend on the image charge and show unfavorable scaling with the number of emitted electrons. Generating a cigar-like electron beam offers improvements for the transverse emittance and 4D brightness at the expense of an increase in the longitudinal emittance and 6D brightness. The degree to which this issue can be mitigated or corrected by using an RF cavity is still an open question. We note again that, while we include the emittance data in our discussion, other quantities, such as the temporal and spatial resolutions at the sample, offer a more robust figure of merit as the rms emittance defined here and used in the literature is not a true constant of motion. Therefore, we also consider peak brightness, coherence length, and energy spread, and show that different operational regimes can be defined depending on the exciting laser pulse characteristics, the extraction field and the number of electrons required. If time resolution is not a concern and for low N_e and F_a (in our simulations represented by $N_e < 5 \times 10^5$ and $F_a = 1$ MV/m), the cigar-like pulse offers a better performance compared to the pancake aspect ratio, whether Gaussian or Elliptical. For applications requiring a higher number of electrons, the extraction field F_a has to be increased to prevent the onset of the unfavorable VC limit. Doing so reduces the advantages of using cigar-like pulses both in terms of coherence length and energy spread and may lead to situations in which the pancake-like pulse with an elliptical profile offers a better compromise. For applications requiring high temporal resolution, a pancake-like pulse with an elliptical radial profile is the option that results in the highest 6D brightness with moderate values of the coherence length and energy spread over a wide range of extracted currents.

ACKNOWLEDGMENTS

We acknowledge support from U.S. National Science Foundation under Grant No. NSF-DMR 1126343 and a seed grant from the MSU Foundation for developing the ultrafast electron microscope. Computational work in support of this research was performed at Michigan State University's High Performance Computing Facility.

[1]M. Aidelsburger, F. O. Kirchner, F. Krausz, and P. Baum, Proc. Natl. Acad. Sci. U. S. A. **107**, 19714 (2010).
[2]R. Akre, D. Dowell, P. Emma, J. Frisch, S. Gilevich, G. Hays, Ph. Hering, R. Iverson, C. Limborg-Deprey, H. Loos, A. Miahnahri, J. Schmerge, J. Turner, J. Welch, W. White, and J. Wu, Phys. Rev. Spec. Top. Accel. Beams **11**, 030703 (2008).
[3]P. Baum, D. S. Yang, and A. H. Zewail, Science **318**, 788 (2007).
[4]C. N. Berglund and W. E. Spicer, Phys. Rev. **136**, A1030 (1964).
[5]H. Boersch, Z. Phys. **139**, 115 (1954).
[6]C. M. Dobson, Nature **426**, 884 (2003).
[7]D. H. Dowell and J. F. Schmerge, Phys. Rev. Spec. Top. Accel Beams **12**, 074201 (2009).
[8]D. Filippetto, P. Musumeci, M. Zolotorev, and G. Stupakov, Phys. Rev. Spec. Top. Accel. Beams **17**, 024201 (2014).
[9]A. Gahlmann, S. T. Park, and A. H. Zewail, Phys. Chem. Chem. Phys. **10**, 2894 (2008).
[10]*Science of Microscopy*, edited by P. W. Hawkes, and J. C. H. Spence (Springer, New York, 2008).
[11]*Classical Electrodynamics*, edited by J. D. Jackson (Wiley, New York, 1998).
[12]X. Jiang, C. N. Berglund, A. E. Bell, and W. A. Mackie, paper presented at the 42nd International Conference on Electron, Ion, and Photon Beam Technology and Nanofabrication (1998), Vol. 16, p. 3374.
[13]W. E. King, G. H. Campbell, A. Frank, B. Reed, J. F. Schmerge, B. J. Siwick, B. C. Stuart, and P. M. Weber, J. Appl. Phys. **97**, 111101 (2005).
[14]O. J. Luiten, S. B. van der Geer, M. J. de Loos, F. B. Kiewiet, and M. J. van der Wiel, Phys. Rev. Lett. **93**, 094802 (2004).
[15]K. Makino and M. Berz, Nucl. Instrum. Methods Phys. Res., Sect. A **558**, 346 (2006).
[16]R. A. Murdick, R. K. Raman, Y. Murooka, and C. Y. Ruan, Phys. Rev. B **77**, 245329 (2008).
[17]P. Musumeci, J. T. Moody, R. J. England, J. B. Rosenzweig, and T. Tran, Phys. Rev. Lett. **100**, 244801 (2008).
[18]P. Musumeci, J. T. Moody, C. M. Scoby, M. S. Gutierrez, and M. Westfall, Appl. Phys. Lett. **97**, 063502 (2010).
[19]J. Portman, H. Zhang, Z. Tao, K. Makino, M. Berz, P. M. Duxbury, and C. Y. Ruan, Appl. Phys. Lett. **103**, 253115 (2013).
[20]R. K. Raman, R. A. Murdick, R. J. Worhatch, Y. Murooka, S. D. Mahanti, T.-R. T. Han, and C. Y. Ruan, Phys. Rev. Lett. **104**, 123401 (2010).
[21]L. M. Rangarajan and G. K. Bhide, Vacuum **30**, 515 (1980).
[22]B. W. Reed, J. Appl. Phys. **100**, 034916 (2006).
[23]B. W. Reed, M. R. Armstrong, N. D. Browning, G. H. Campbell, J. E. Evans, T. LaGrange, and D. J. Masiel, Microsc. Microanal. **15**, 272 (2009).
[24]C. Y. Ruan, Y. Murooka, R. K. Raman, R. A. Murdick, R. J. Worhatch, and A. Pell, Microsc. Microanal. **15**, 323 (2009).
[25]C. Y. Ruan, F. Vigliotti, V. A. Lobastov, S. Chen, and A. H. Zewail, Proc. Natl. Acad. Sci. U. S. A. **101**, 1123 (2004).
[26]G. Sciaini and R. J. Dwayne Miller, Rep. Prog. Phys. **74**, 096101 (2011).
[27]B. J. Siwick, J. R. Dwyer, R. E. Jordan, and R. J. Dwayne Miller, J. Appl. Phys. **92**, 1643 (2002).
[28]R. Srinivasan, V. A. Lobastov, C. Y. Ruan, and A. H. Zewail, Helv. Chim. Acta **86**, 1761 (2003).
[29]T. Srinivasan-Rao, J. Fischer, and T. Tsang, J. Appl. Phys. **69**, 3291 (1991).
[30]Z. Tao, H. Zhang, P. M. Duxbury, M. Berz, and C. Y. Ruan, J. Appl. Phys. **111**, 044316 (2012).
[31]A. Valfells, D. W. Feldman, M. Virgo, P. G. O'Shea, and Y. Y. Lau, Phys. Plasmas **9**, 2377 (2002).
[32]T. van Oudheusden, P. L. E. M. Pasmans, S. B. van der Geer, M. J. de Loos, M. J. van der Wiel, and O. J. Luiten, Phys. Rev. Lett. **105**, 264801 (2010).
[33]A. H. Zewail and J. M. Thomas, *4D Electron Microscopy: Imaging in Space and Time* (Imperial College Press, London, 2010).
[34]H. Zhang and M. Berz, Nucl. Instrum. Methods Phys. Res., Sect. A **645**, 338 (2011).